ELSEVIER

Contents lists available at ScienceDirect

Journal of Alloys and Compounds

journal homepage: http://www.elsevier.com/locate/jalcom



Intriguing luminescence properties of (Ba, Sr)₃Si₆O₉N₄: Eu²⁺ phosphors via modifying synthesis method and cation substitution



Liang-Jun Yin ^{a, d, *, 1}, Wei-Wei Ji ^{b, 1}, Shi-Yu Liu ^a, Wei-Dong He ^a, Lin Zhao ^a, Xin Xu ^b, Andrea Fabre ^c, Benjamin Dierre ^d, Ming-Hsien Lee ^e, J. Ruud van Ommen ^c, Hubertus T. (Bert) Hintzen ^{d, **}

- a School of Energy Science and Engineering, University of Electronic Science and Technology of China, 2006 Xiyuan Road, Chengdu, PR China
- b Laboratory of Materials for Energy Conversion, Department of Materials Science and Engineering, University of Science and Technology of China, Hefei, PR China
- c Department of Chemical Engineering, Faculty of Applied Sciences, Delft University of Technology, Julianalaan 136, 262 Delft, The Netherlands
- d Luminescent Materials Research Group, Faculty of Applied Sciences, Delft University of Technology, Mekelweg 15, 2629 JB Delft, The Netherlands
- ^e Department of Physics, Tamkang University, Tamsui, Taipei 251, Taiwan

ARTICLE INFO

Article history: Received 25 March 2016 Received in revised form 29 April 2016 Accepted 2 May 2016 Available online 3 May 2016

Keywords: (Ba, Sr)₃Si₆O₉N₄: Eu²⁺ Phosphor Blueshift Second-sphere shrinkage Local structure disordering

ARSTRACT

Synthesizing pure phase $Ba_3Si_6O_9N_4$ by the conventional solid-state reaction method is challenging because of easily formed secondary phase $Ba_3Si_6O_{12}N_2$ showing similar crystal structure. In this work, an alternative low temperature synthesis method is presented, and a series of green to blue emitting (Ba, $Sr)_3Si_6O_9N_4$: Eu^{2+} phosphors were prepared by a mechanochemical activation route. Variations in photoluminescence properties and crystal structure, as induced by the change in phosphor composition, were investigated. Under ultraviolet-light excitation, $Ba_3Si_6O_9N_4$: Eu^{2+} phosphor exhibited a strong narrow green emission at 518 nm and simultaneously a weak emission at 405 nm, which are ascribed to different Eu/Ba sites in $Ba_3Si_6O_9N_4$ lattice proved by Density Functional Theory (DFT) calculations. A continuous green to blue emission in (Ba, $Sr)_3Si_6O_9N_4$: Eu^{2+} phosphors could be achieved by tuning the crystal structure and local coordination environment acting on Eu^{2+} with Eu/Ba substitution. More Eu/Ba substitution improved thermal quenching and resulted in a different characteristic of emission peak shift upon increasing the temperature.

 $\ensuremath{\text{@}}$ 2016 Elsevier B.V. All rights reserved.

1. Introduction

As excellent candidates for phosphor-conversion white-LEDs, rare earth-doped (oxy)nitride phosphors have attracted considerable attention due to their nontoxicity, pronounced flexibility for materials design and robust thermal stability [1–6]. In particular, red-emitting phosphors $M_2Si_5N_8$: Eu^{2+} (M = Ca, Sr, and Ba) and CaAlSiN₃: Eu^{2+} , yellow-emitting phosphor Ca-a-SiAlON: Eu^{2+} and green-emitting phosphor β -SiAlON: Eu^{2+} have been successfully commercialized [7–12]. Current studies are mostly focused on the

synthesis of novel oxonitridosilicates as host systems. In this regard, the structure and luminescence of a novel Ba₃Si₆O₉N₄: Eu²⁺ phosphor material has been recently studied [13,14]. Ba₃Si₆O₉N₄ crystallizes as a trigonal structure and when doped with Eu²⁺ gives a green emission peaking at ~520 nm under UV excitation, which allows this phosphor to be suitable for application in white LEDs excited by UV or near-UV. However, it still remains challenging to synthesize single-phase Ba₃Si₆O₉N₄: Eu²⁺ by the direct conventional solid-state reaction method (SSR) and moreover study of the evolution of phosphor properties with Sr²⁺ substitution for Ba²⁺ ions in Ba₃Si₆O₉N₄ host has not yet been reported. In addition, the process of SSR generally requires higher temperature and longer holding time, which is energy-consuming. A post-grinding step to pulverize hard agglomerates into fine powder is required due to the high temperature used. Therefore, it is necessary to seek alternative low temperature synthesis methods to achieve pure Ba₃Si₆O₉N₄ phase and research the properties of these resulting phosphors.

^{*} Corresponding author. School of Energy Science and Engineering, University of Electronic Science and Technology of China, 2006 Xiyuan Road, Chengdu, PR China.

^{**} Corresponding author.

E-mail addresses: ylj@mail.ustc.edu.cn (L.-J. Yin), h.t.hintzen@tudelft.nl

¹ Liang-Jun Yin and Wei-Wei Ji contributed equally to this paper.

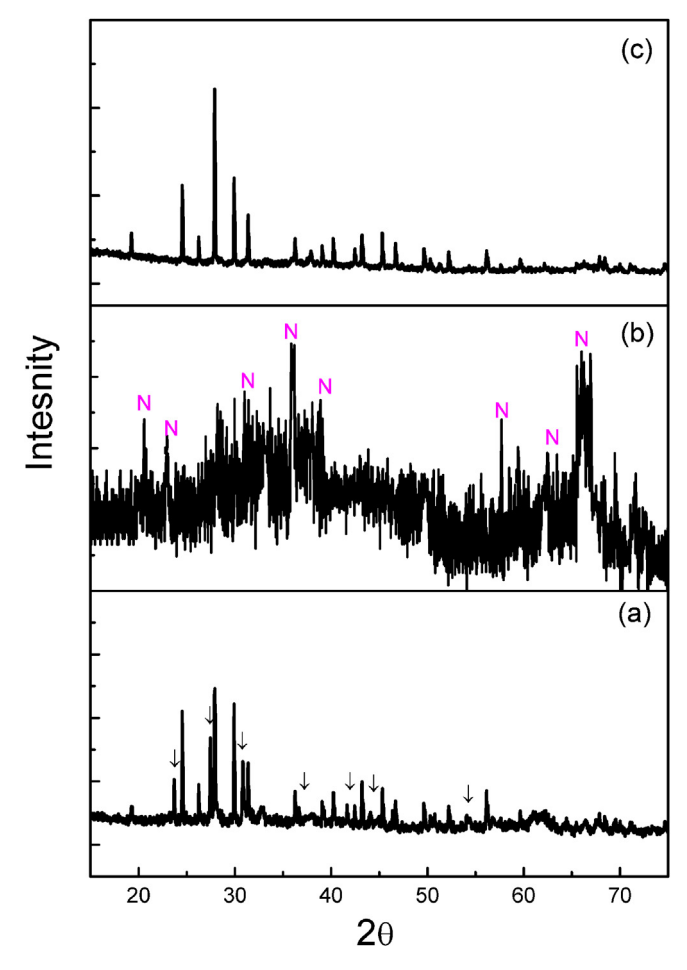


Fig. 1. XRD patterns of $Ba_3Si_6O_9N_4$: Eu^{2+} synthesized by conventional solid-state reaction at 1450 °C for 4 h in nitrogen (a), precursors after high-energy ball milling (b), sample b annealed at 1200 °C for 4 h in nitrogen (c). \downarrow and N represent $Ba_3Si_6O_{12}N_2$ and Si_3N_4 phase respectively.

High-energy ball milling (HEBM) is a powder-based processing synthetic method. The starting powders used for HEBM are transformed during milling into an amorphous phase with homogenous distribution of elements and in addition the powder sizes are reduced substantially to achieve a high reactivity [15–17]. On account of such advantages, this technique has allowed for the efficient synthesis of certain oxynitride materials [18–20], which are difficult to prepare by other methods.

In this work, $(Ba, Sr)_3Si_6O_9N_4$: Eu^{2+} blue/green-emitting phosphors with a single phase are synthesized with HEBM method and the structure and luminescence properties of $(Ba, Sr)_3Si_6O_9N_4$: Eu^{2+} phosphors are investigated. To clarify the origin of the green/blue light, we perform DFT + U calculations to obtain the electronic structure of $Ba_3Si_6O_9N_4$: Eu^{2+} . Our work indicates that Eu^{2+} ions occupy different Ba sites with high and low probability, resulting in strong and weak emission intensity, respectively.

2. Material and methods

Powders with a nominal composition (Ba, Sr)_{2.85}Si₆O₉N₄: 0.15Eu²⁺ were synthesized by solid-state reaction with and without HEBM. BaCO₃ (Sinopharm Chemical Reagent Co. Ltd, Shanghai, China), SrCO₃ (Sinopharm Chemical Reagent Co. Ltd, Shanghai, China), Eu₂O₃ (Sinopharm Chemical Reagent Co. Ltd, Shanghai, China), Si₃N₄ (96.0%, UBE Industries, Ltd, Japan) and SiO₂

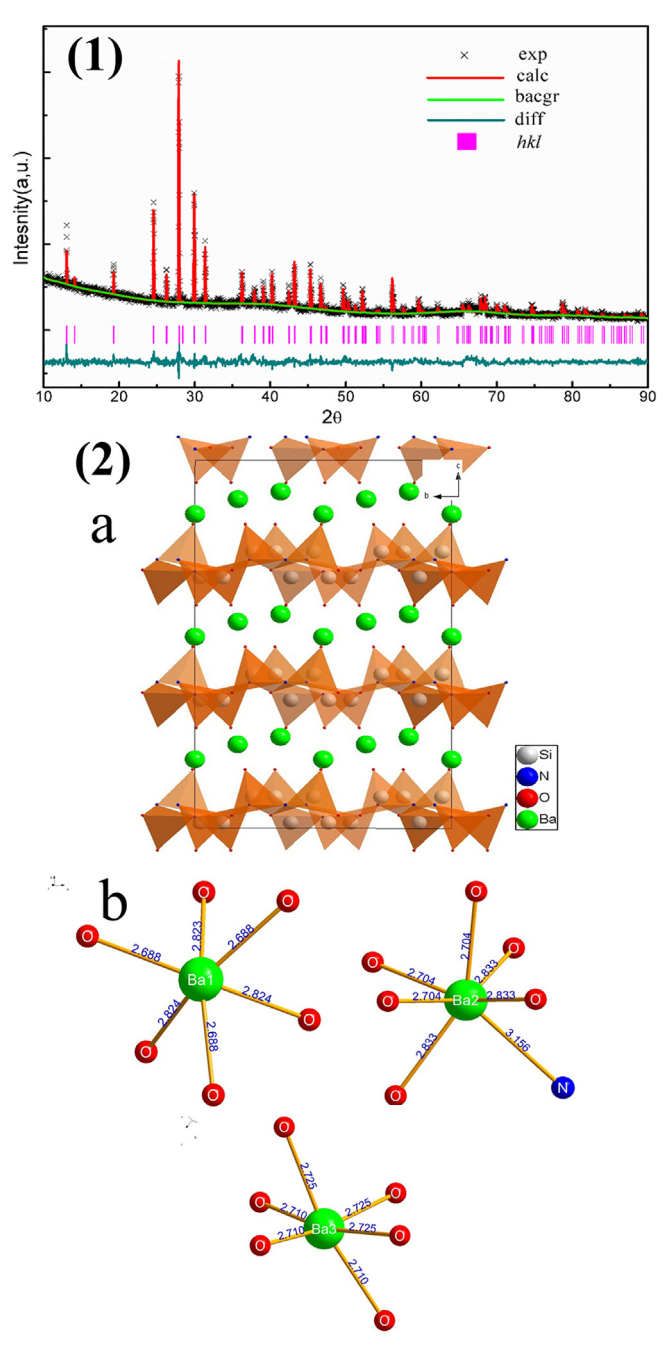


Fig. 2. (1) Rietveld refinement of crystal structure of un-doped $Ba_3Si_6O_9N_4$ prepared by HEBM method. Observed, calculated, background and difference signal, and hkl of the XRD pattern are plotted in the same range. (2) a. A view of the $Ba_3Si_6O_9N_4$ crystal structure along (001) direction; b. Coordination environments of three types of Ba^{2+} ions in $Ba_3Si_6O_9N_4$.

(Sinopharm Chemical Reagent Co. Ltd, Shanghai, China, 99.99%) were wet mixed in ethanol using Si_3N_4 balls at a milling speed of 300 rpm for 12 h (QM-3SP2, Nanda Instrument Co. Ltd, Nanjing, China). After drying the mixed powders were mechanically milled with high energy (PM-1200, Seishin Enterprise Co., Ltd., Japan) in a 350 mL silicon nitride pot with 5 mm silicon nitride balls. The ball-to-powder weight ratio was 10:1 at a milling speed of 900 rpm and milling time was 4 h. Finally the precursors were annealed in BN crucibles under N_2 atmosphere for 4 h at 1200 °C. More details are given in our previous report [21,22].

The phase formation was analyzed by an X-ray diffractometer

(Model PW 1700, Philips Research Laboratories, Eindhoven, The Netherlands) using Cu Kα radiation at a scanning rate of 2°/min for phase information and 0.1°/min for Rietveld refinement. The XRD refinement was performed using the Rietveld method in Reflex tools in Materials Studio. The lattice parameters were calculated using Unit Cell software based on XRD diffraction angles. The inner structure was observed by High-Resolution Transmission Electron Microscopy (HRTEM) (Model 2100F, IEOL, Tokyo, Japan), Energy-Dispersive X-day Spectroscopy (EDS) measurements were performed at room temperature in a scanning electron microscope (JSM-6390LA, JEOL, Japan). Photoluminescence spectra were obtained by a fluorescent spectrophotometer (Model F-4600, Hitachi, Tokyo, Japan) with a 200 W Xe lamp as an excitation source. The emission spectrum was corrected for the spectral response of the monochromator and Hamamatsu R928P photomultiplier tube (Hamamatsu Photonics K.K., Hamamatsu, Japan) by a light diffuser and tungsten lamp (Noma Electric Corp., NY; 10V, 4A). The excitation spectrum was also corrected for the spectral distribution of the xenon lamp intensity by measuring Rhodamine-B as a reference. The temperature dependent luminescence measurement was conducted on the fluorescent spectrophotometer equipped with a high temperature fluorescence controller (Model TAP-02, KOJI instrument Co. Ltd, Tianjin, China). Diffuse-reflectance spectra were measured at room temperature by a UV-Vis-NIR spectrophotometer (Model CARY 5000, Agilent Technologies, USA) equipped with an integrating sphere (Model Internal DRA-2500, Agilent Technologies, USA).

Our first principles calculations were based on Density Functional Theory (DFT) within the Generalized Gradient Approximation (GGA) proposed by Perdew, Burke, and Ernzerhof (PBE) [23] using the CASTEP code [24,25]. The code used the iterative diagonalization technique to minimize the total energy with respect to the plane-wave coefficients. The ultrasoft pseudopotentials used for all atoms were those supplied by Accelrys. A cutoff energy of 480 eV was used to limit the total energy convergence within 0.1 eV per atom. Here, 88-atoms (i.e. a supercell with formula units $Ba_3Si_6O_9N_4$: Eu^{2+}) was used in the calculations. The k-point samplings for the supercells were $2 \times 1 \times 2$, according to the Monkhorst-Pack scheme [26], which generates 16 irreducible kpoints, respectively, in the irreducible Brillouin zone (BZ). The parameters for convergence control of the geometry optimization were 1×10^{-5} eV/atom for total energy, 0.03 eV/Å for maximum force, 0.05 GPa for stress, and 0.001 Å for displacement. The Self-Consistent Field (SCF) energy convergence threshold was set as 1×10^{-6} eV/atom to ensure the accuracy of the electronic calculation. The electron correlation associated with the f orbitals of Eu was treated in a mean field approach by adding an effective Hubbard on-site repulsion $U_{eff}=2\ eV$ on Eu 4f obitals. This GGA + U treatment was necessary to properly describe the absorption edge of rare-earth containing materials. It should be noted that our absorption edge calculation results are not sensitive to Ueff.

3. Results and discussion

3.1. Ba₃Si₆O₉N₄: Eu²⁺

From the XRD patterns the Eu doped sample synthesized by conventional SSR at the firing temperature of 1450 °C for 4 h in nitrogen consists of Ba₃Si₆O₉N₄ (JCPDS card number: 415918, a = 7.249 Å, c = 6.784 Å) and a small amount of Ba₃Si₆O₁₂N₂ impurity (Fig. 1(a)). This result shows that pure Ba₃Si₆O₉N₄ phase cannot be obtained by this direct method and there is present a secondary phase Ba₃Si₆O₁₂N₂ in the final product due to their similar crystal structure and same Ba/Si ratio, as consistent with the previous report [13].

With HEBM, XRD peaks of the starting powders are significantly weakened and broadened, while a highly amorphous background is observed as shown in Fig. 1(b). Due to the strong connecting covalent bond between Si (electronegativity: 1.98) and N (electronegativity: 3.04), it is difficult to destroy the Si₃N₄ crystal lattice. As a result, weakened XRD peaks still appear, which is ascribed to some remaining crystalline Si₃N₄ in the precursor. This indicates that the HEBM method efficiently transforms most of the powders into an amorphous state with a uniform atomic distribution and a high reactivity. For the annealing temperature of 1200 °C, which is significantly lower than 1450 °C required for direct SSR, un-doped Ba₃Si₆O₉N₄ as well as Ba₃Si₆O₉N₄: Eu²⁺ phosphors with a single phase trigonal structure are achieved as shown in Fig. 1(c).

Quantitative composition analysis using EDS shows that the undoped Ba₃Si₆O₉N₄ sample is composed of Ba, Si, N and O, with the atomic ratios of Ba/Si of 1:1.8 (Fig. S1, Supporting Information), which is close to the stoichiometric Ba₃Si₆O₉N₄, indicating that part of Si is lost in the high temperature firing process. The refined crystal structure and X-ray diffraction (XRD) pattern of Ba₃Si₆O₉N₄ are presented in Fig. 2-(1). The structure of Ba₃Si₆O₉N₄ is refined applying the Rietveld method on the XRD data and the detailed refinement parameters are listed in Table S1 (Supporting Information). Rietveld refinement parameters ($R_P = 6.02\%$, $R_{WP} = 7.83\%$) confirm the high purity of Ba₃Si₆O₉N₄ via the HEBM method. Ba₃Si₆O₉N₄ is constructed by corner sharing Si(O,N)₄ tetrahedra forming corrugated layers (Fig. 2-2a), between which the Ba²⁺ ions are located. As shown in Fig. 2-(2b), the Ba²⁺ ions occupy three different crystallographic sites: two of them are trigonal antiprisms with six oxygen atoms, and the third one is trigonal antiprism with six oxygen atoms, further capped with a nitrogen atom. Because of the similarities of their ionic radii, the Eu²⁺ is expected to randomly occupy these three Ba²⁺ ion sites in the Eu doped Ba₃Si₆O₉N₄ crystal. If the above deduction is correct, several emission bands may be observed due to the different local crystal

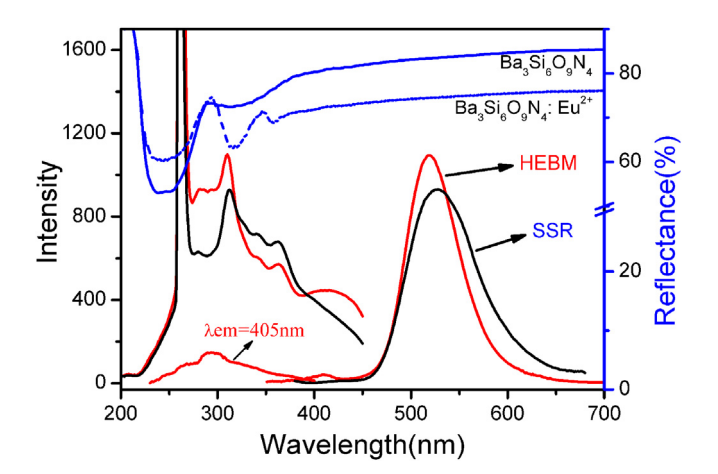


Fig. 3. Excitation and emission spectra of Ba₃Si₆O₉N₄:Eu²⁺ synthesized by SSR ($\lambda_{ex}=315$ nm, $\lambda_{em}=525$ nm) and HEBM ($\lambda_{ex}=315$ nm, $\lambda_{em}=518$ nm). The strong sharp signal in the excitation spectrum at about 260 nm is due to no use of the correct filter, as a consequence of which second order radiation is transmitted. The reflection spectra of Ba₃Si₆O₉N₄ and Ba₃Si₆O₉N₄: Eu²⁺ are also shown in this figure.

Table 1 Eu $4f \rightarrow 5d$ Transition energy and relative total energy of BSON:Eu.

	Transition energy (eV)	Relative total energy (meV)
BSON:Eu1	3.34	-13
BSON:Eu2	3.34	0
BSON:Eu3	3.10	-75

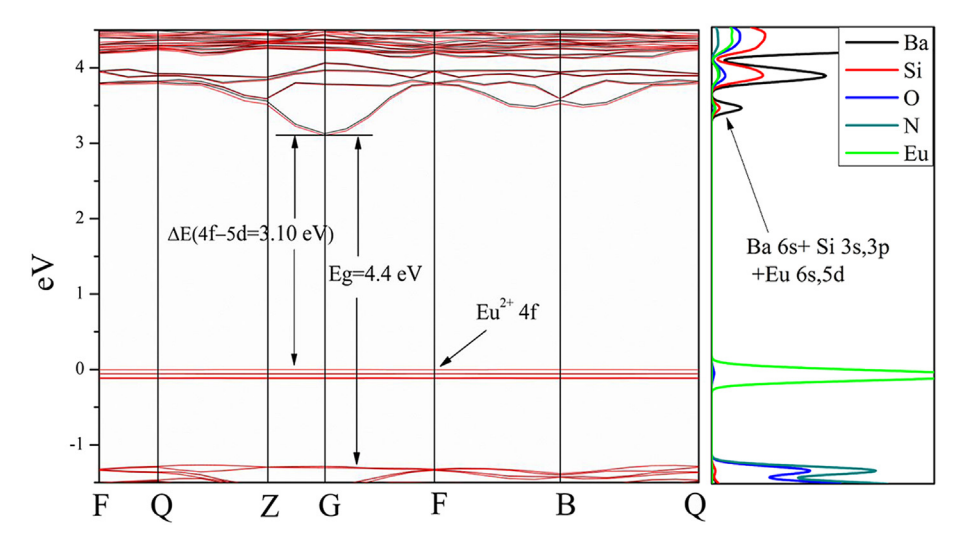


Fig. 4. Band structures and DOS of Ba₃Si₆O₉N₄: Eu3 (Fermi surface is set to zero).

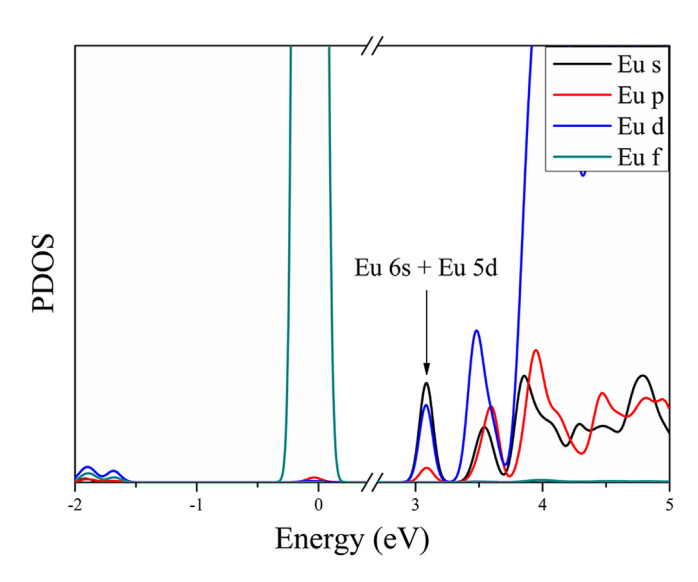


Fig. 5. PDOS (partial density of states) of Eu in $Ba_3Si_6O_9N_4$: Eu3 from -2 to 5 eV.

fields acting on Eu²⁺ [8], [27]. As it is well known, the lowest 5d energy level of Eu²⁺ is strongly influenced by the nephelauxetic effect and crystal-field splitting. Nitrogen is less electronegative and more polarizable than oxygen. The nitrogen-metal bonds are thus more covalent and lower 5d energy level. Based on the crystal field splitting (CFS) theory, the crystal field acting on central ions can be expressed as $Dq = 35Ze/4R^5$, where Z is the valence of anions, e is elementary charge and R is the distance between central cation and coordinating anions. Therefore, three different Eu coordinations are expected to result in three different emission peaks, which leads to the overlap of different emission peaks and consequently a broad asymmetric emission band.

Fig. 3 shows the optical properties of $Ba_3Si_6O_9N_4$: Eu^{2+} phosphors synthesized by SSR and HEBM method respectively, at room temperature. For the phosphors prepared by the HEBM method, two absorption bands are observed in the reflection spectrum with minima at ~240 nm, 320 nm and smaller peak at 360 nm, respectively. The first band is assigned to the absorption of the host lattice and the others correspond to $4f^7 \rightarrow 4f^65d$ transitions of Eu^{2+} . The excitation spectra show a broad band with some fine structure ranging from 250 nm to 400 nm, and both phosphors exhibit a

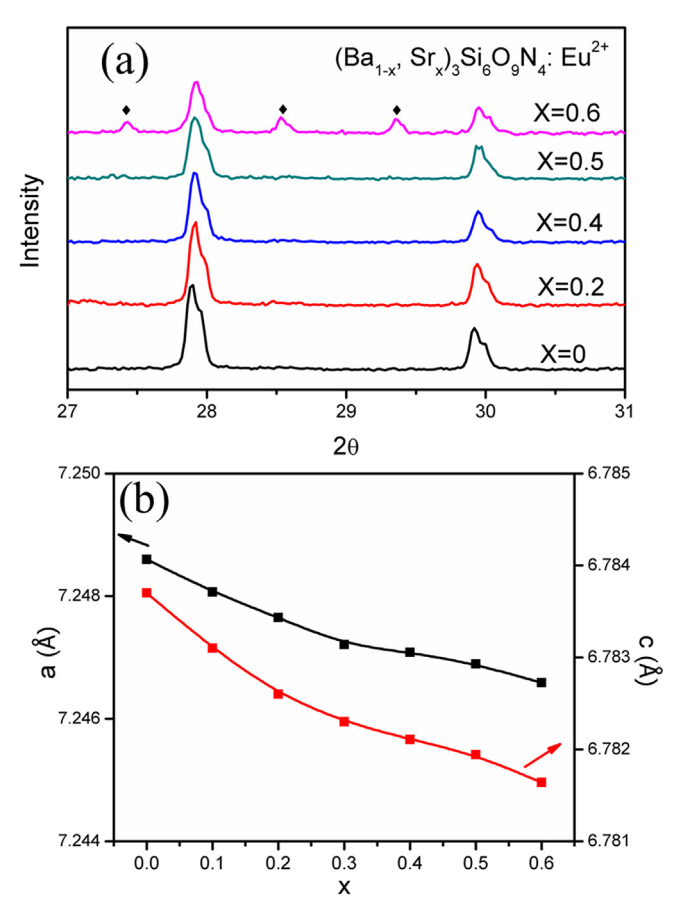


Fig. 6. XRD patterns and lattice parameters of $(Ba_{1-x}, Sr_x)_3Si_6O_9N_4$: Eu²⁺ as a function of x. Filled diamonds represent unknown phase.

green emission band centered at 518 nm (HEBM) and 525 nm (SSR) under 315 nm excitation. The observed full width at half maximum (FWHM) 59 nm in phosphors by HEBM is much smaller than that by SSR (82 nm). As shown in Fig. 1, the phosphors by SSR are composed of major Ba₃Si₆O₉N₄ phase and Ba₃Si₆O₁₂N₂ impurity. In fact, the crystal structure and chemical formula of Ba₃Si₆O₉N₄ (trigonal, a = 7.249 Å, c = 6.784 Å) appear close to Ba₃Si₆O₁₂N₂ (trigonal, a = 7.505 Å, c = 6.597 Å) [28]. Since the Ba–N bond length in

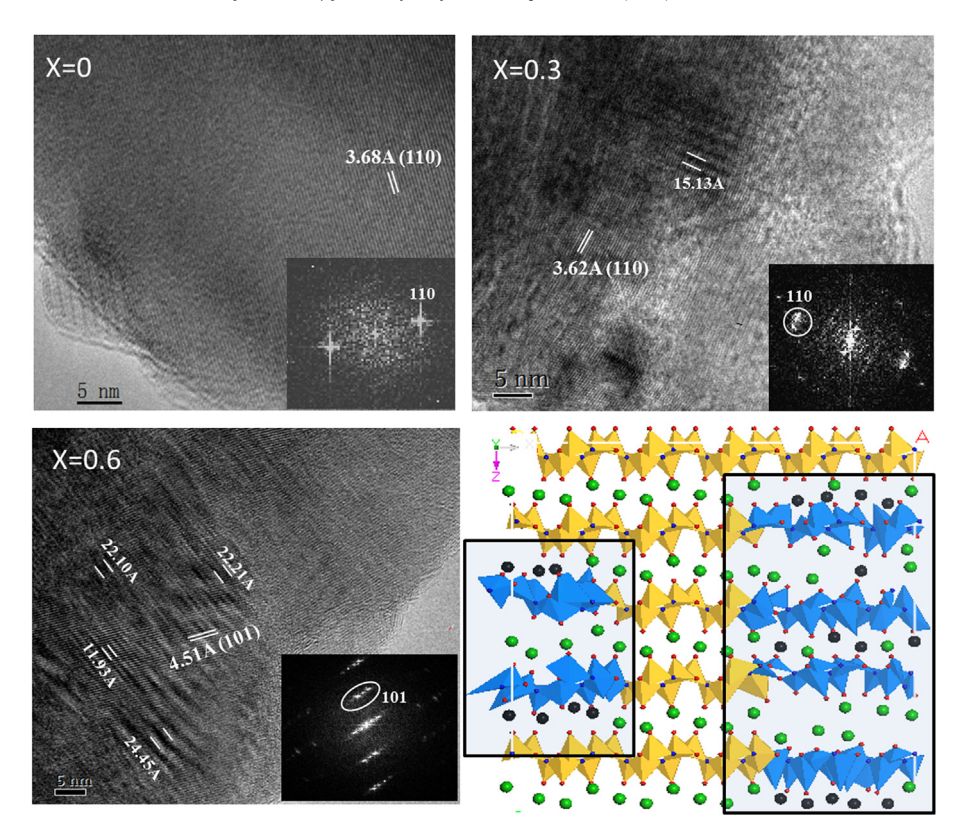


Fig. 7. HRTEM images $(Ba_{1-x}, Sr_x)_3Si_6O_9N_4$: Eu²⁺ samples (x = 0, 0.3 and x = 0.6). |The inset shows FFT calculated from corresponding HRTEM images. Structure model shows Sr doping distorts local structure, appearing blue in the rectangle. Black balls represent Sr atom and others are same to Fig. 2-(2). (For interpretation of the references to colour in this figure legend, the reader is referred to the web version of this article.)

Ba₃Si₆O₁₂N₂: Eu²⁺ (~3.0 Å) is smaller than that in Ba₃Si₆O₉N₄: Eu²⁺ (~3.2 Å) [28], the crystal field splitting of Eu²⁺ 5d levels in Ba₃Si₆O₁₂N₂: Eu²⁺ is larger than that in Ba₃Si₆O₉N₄: Eu²⁺. It has been reported that Ba₃Si₆O₁₂N₂: Eu²⁺ phosphors show an emission wavelength of 530 nm [29], which is slightly longer than that of Ba₃Si₆O₉N₄: Eu²⁺ phosphor. As a result, the overall emission band in the phosphors obtained by SSR is shifted to somewhat higher wavelength as well as broadened due to the overlap of emission bands of Ba₃Si₆O₉N₄: Eu²⁺ (518 nm) and Ba₃Si₆O₁₂N₂: Eu²⁺ (530 nm) phosphors. In addition, a weak emission at 405 nm is observed in Ba₃Si₆O₉N₄: Eu²⁺ phosphors by HEBM method (Fig. 3), which will be discussed later.

As discussed earlier, a broad inhomogeneous emission band should be observed if Eu^{2+} ions randomly occupy the three Ba^{2+} ion sites available in the Eu doped $Ba_3Si_6O_9N_4$ crystal structure, as shown in Fig. 2-2b. From Fig. 3, it should be noted that $Ba_3Si_6O_9N_4$: Eu^{2+} phosphors exhibit a symmetric emission spectrum. Theoretical calculations are then performed in this work to elucidate such an inconsistency.

We built models of Ba₃Si₆O₉N₄ with the Ba(1) site replaced with Eu (BSON: Eu1 for simplification). Similarly, other models, like BSON: Eu2 and BSON: Eu3 were also established. In our calculations, we first carried out full geometry relaxations for the three models and then calculated the single-point energy, density of state and band structure of them. Table 1 shows the Eu 4f-5d transition energy as well as relative total energy of BSON with Eu in different sites. By comparing the relative total energy of Eu in different sites of BSON, BSON: Eu3 configuration is considered to be the most stable among them.

Fig. 4 presents the band structures and Density of States (DOS) of BSON: Eu3. The results reveal that BSON has a direct bandgap of ~4.4 eV, which is smaller than the absorption edge 5.20 eV

estimated from the reflection spectrum measured for BSON without ${\rm Eu}^{2+}$ doping (Fig. 3), due to the well-known bandgap underestimation in traditional DFT.

Fig. 5 shows the atom-resolved partial DOS (PDOS) for Eu in BSON: Eu3. The Eu 4f energy levels emerge on the Fermi surface and the majority spin states (spin \uparrow) of Eu are fully occupied. The peak of the Eu 5d and Eu 6s states appears at 3.10 eV above the Fermi level (Fig. 4). Unlike the localized Eu 4f orbitals as illustrated, the Eu 5d orbitals expand in the entire conduction band and hybridize with Ba 6s, Si 3s, 3p, and Eu 6s states at the bottom of conduction band. However, the optical transition between the Eu²⁺ 4f ground state to 6s state is forbidden. Hence, we consider that the lowest energy transition mainly occurs between the Eu²⁺ 4f and 5d states at the bottom of the conduction band. The band structure and DOS of BSON: Eu1 and BSON: Eu2 are similar to those of BSON: Eu3 (Fig. S2, Supporting Information).

As presented in Table 1, it can be observed that BSON: Eu3 has a Eu $4f \rightarrow 5d$ transition energy of 3.10 eV, which is rather close to the experimentally observed maximum at about 420 nm (2.95 eV) in the excitation spectrum (Fig. 3) monitored at 518 nm. BSON: Eu1 and BSON: Eu2 have Eu $4f \rightarrow 5d$ transition energies of 3.34 eV, both of which are substantially closer to the experimental excitation band maxima of 376 nm (3.30 eV) monitored at 405 nm than BSON: Eu3. Accordingly, we ascribe the emission peak at 518 nm to the Eu in Ba(3) sites and that at 405 nm to the Eu in Ba(1) and Ba(2) sites. These suggestions are also supported by the values of the relative total energy of Eu in different Ba sites of BSON. The relative total energy of BSON: Eu increases in the order BSON: Eu3, BSON: Eu1 and BSON: Eu2. Consequently, Eu $^{2+}$ should be strongly prone to be located at the Ba(3) site, which may explain why the emission peak at 518 nm is much stronger than that at 405 nm.

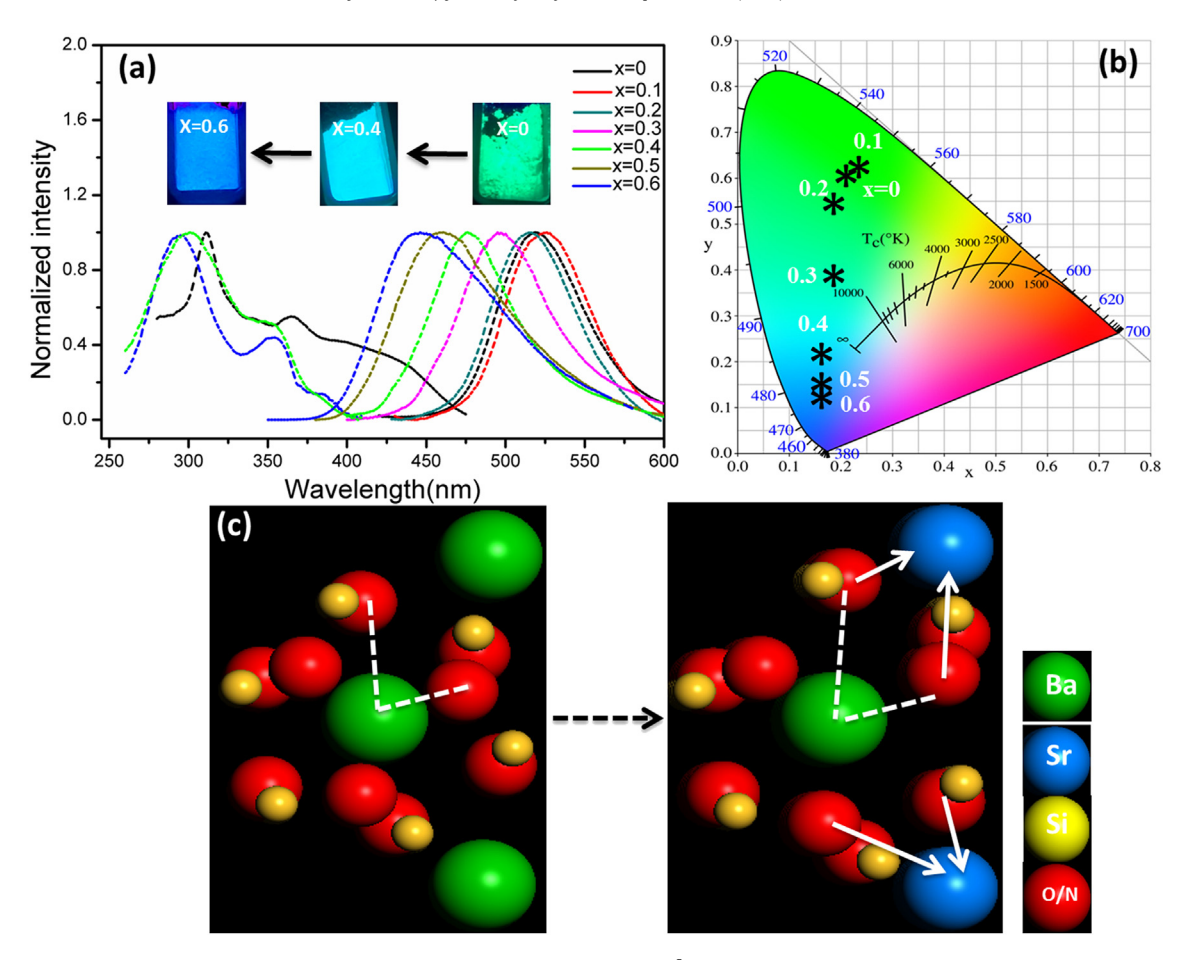


Fig. 8. a. Excitation and emission spectra. b. CIE chromaticity positions for $(Ba_{1-x}, Sr_x)_3Si_6O_9N_4$: Eu^{2+} phosphors as a function of x. c. Schematic neighboring-cation effect for the activator ion without and with Sr/Ba replacement.

3.2. $(Ba, Sr)_3Si_6O_9N_4$: Eu^{2+}

In this part, the structure and luminescence properties are also studied in terms of effects of Sr substitution for Ba^{2+} ions in $(Ba_{1-x},Sr_x)_3Si_6O_9N_4$ host. Fig. 6-a shows the XRD patterns of synthesized powders with the composition of $(Ba_{1-x},Sr_x)_3Si_6O_9N_4\colon Eu^{2+}$. The $(Ba_{1-x},Sr_x)_3Si_6O_9N_4\colon Eu^{2+}$ samples appear to be solid solutions throughout the x=0-0.5 range. Some unknown impurities gradually appear with further increase of Sr content. Meanwhile, with an increase of Sr/Ba substitution, the XRD diffraction intensity decreases, indicating that the crystallinity of $(Ba_1Sr)_3Si_6O_9N_4$ turns worse. The reason should be the substitution of Sr for Ba partly destroys the periodic structure of $Ba_3Si_6O_9N_4$ crystal lattice.

With the increase of Sr content, the major diffraction peaks at ~27.9° and 29.9° shift to a higher angle, indicating that Sr/Ba substitution leads to a decrease of crystal lattice parameters. As shown in Fig. 6-b, it is seen that the hexagonal lattice parameters of $Ba_3Si_6O_9N_4$ are decreased as Sr contents increase. This crystal lattice reduction is ascribed to the ionic radii discrepancy of 15% between Sr^{2+} (112 pm) and Ba^{2+} (134 pm).

In order to understand the structural change after Sr doping, we imaged these samples using a HRTEM in Fig. 7. The d-spacing directly measured from the HRTEM image are 3.68 (x=0), 3.62 (x=0.3) and 4.51 (x=0.6) Å, which can be indexed to the (110), (110) and (101) planes, respectively. Compared with the standard d-spacing of Ba₃Si₆O₉N₄, the value decreases after Sr/Ba substitution, also indicating the lattice contraction. The HRTEM images of the (Ba_{1-x}, Sr_x)₃Si₆O₉N₄: Eu²⁺ samples (x=0.3, x=0.6) differ from

sample (x = 0) by displaying obvious stacking faults. The stacking faults produce domains across 4-25 Å without regular spacing. In the corresponding Fast Fourier transform images (FFT), one can see that there is streaking of reflections caused by the stacking faults [30]. We interpret the stacking faults as evidence for local regions lacking the symmetry of trigonal structure. The local symmetry loss is the result of abundant stacking faults in (Ba_{1-x}, Sr_x)₃Si₆O₉N₄: Eu^{2+} samples (x = 0.3, x = 0.6). The stacking faults interrupts the periodic structure of Ba₃Si₆O₉N₄ crystal lattice, which explains the weaken XRD diffraction intensity with the increase of Sr concentration in (Ba_{1-x}, Sr_x)₃Si₆O₉N₄: Eu²⁺ phosphors. A structure model in Fig. 7 in a stacking faults region is predicted to explain the broken periodic structure. Due to the mismatch of ionic radius and covalence between Sr²⁺ and Ba²⁺, Sr²⁺ ions will largely attract the surrounding O/N ions and distort the local structure. The local arrangements of atoms across the stacking faults give rise to local structure disordering of Ba₃Si₆O₉N₄ lattice and obviously lowers the symmetry of trigonal structure. It should be noted that this disordered structure is only limited no more than 25 Å (about 4 times of crystal cells), which indicates possible formation of Sr-rich nanosegregation region [31].

Excitation and emission spectra of $(Ba_{1-x}, Sr_x)_3Si_6O_9N_4$: Eu^{2+} are shown in Fig. 8-a. The emission peaks shift toward the longer wavelength region (from 515 nm to 526 nm) with increasing Sr concentrations for low x values (x < 0.1), but for higher Sr contents a slight blue-shift trend is observed. The emission positions in the standard CIE chromaticity diagram are indicated on Fig. 8-b. A notable range of green to blue emitted phosphors is observed with

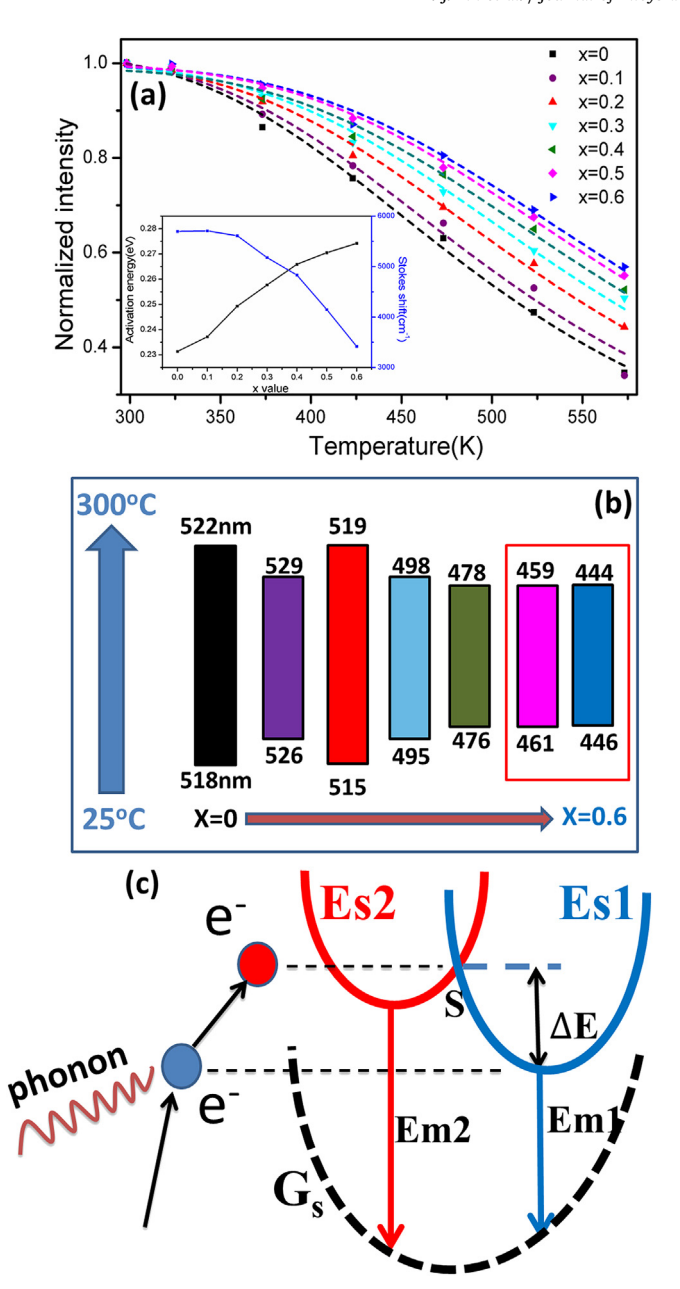


Fig. 9. a. Thermal quenching data for $(Ba_{1-x}, Sr_x)_3Si_6O_9N_4$: Eu^{2+} phosphors as a function of x. Dotted line shows the fitted results according to Arrhenius equation. The inset figure is the change of Stokes shift and activation energy for thermal quenching with x. b. temperature-dependent emission peak shift of $(Ba_{1-x}, Sr_x)_3Si_6O_9N_4$: Eu^{2+} phosphors with x. c. a sketch map showing thermally active phonon-assisted tunneling of Eu^{2+} from low-energy to high-energy state.

x in $(Ba_{1-x}, Sr_x)_3Si_6O_9N_4$: Eu^{2+} phosphor. The emission red-shift is well consistent with the expectation from the decrease of crystal lattice volume with x, which leads to a stronger crystal field acting on Eu^{2+} . Similar shifts are observed in some other nitrides, for example from a 585 nm peak emission for $Ba_2Si_5N_8$: Eu^{2+} to 620 nm for isostructural $Sr_2Si_5N_8$: Eu^{2+} [8,32]. However, the blueshift observed for x > 0.1 appears anomalous given the above arguments. The reason for this phenomenon can be attributed to the following factors. When Sr^{2+} ions are doped into the host lattice, because of the smaller ion radius of Sr^{2+} , on one hand, it will lead to the lattice contraction, leading to a red-shift of emission which is verified by XRD and HRTEM results. On the other hand, to release lattice strain, it will attract the surrounding ions resulting in the

average longer Eu-(O,N) bonds, i.e expansion effect for the activator site by Sr²⁺ substitution for Ba²⁺ in the second sphere in (Ba, Sr)₃Si₆O₉N₄: Eu²⁺ phosphor, as shown in Fig. 8-c [33]. Therefore, these two factors are competitive and determine the emission shift in the phosphor. As x is below 0.1, the effect of lattice contraction is dominant, which gives rise to a larger crystal field splitting. Consequently, a red-shift occurs, Nevertheless, for higher Sr content the effect of the lattice contraction is outweighed by the overall second-sphere shrinkage effect of replacing Ba²⁺ by Sr²⁺, resulting in a blue-shift of emission. However, we don't believe that single neighboring cation effect could be so big to cause an 80 nm emission blue-shift. Possibly, a large low-symmetry structure induced by Sr doping lowers the crystal field acting on Eu²⁺ from which an emission blue-shift originates. This phenomenon indicates that the 5d-orbital crystal field splitting of Eu²⁺ gradually decreases with increasing x (x > 0.1), supporting the proposed emission blue-shift mechanism.

The high thermal quenching behavior of the photoluminescence is undesirable for applications in phosphors-converted white LEDs. Fig. 9-a shows the temperature-dependent emission intensity of (Ba, Sr)₃Si₆O₉N₄: Eu²⁺ phosphors from 25 °C to 300 °C. The thermal stability is improved due to Sr²⁺ substitutions for Ba²⁺. At a working temperature of about 150 °C for white LEDs, the emission intensity of the phosphors with composition (x = 0), (x = 0.2), and (x = 0.4) maintains 75%, 80%, and 84% versus the emission intensity at room temperature, respectively. They are fitted according to the Arrhenius equation associated with temperature-dependent emission intensity [34]:

$$I(T) = \frac{I_0}{1 + Ae^{-\frac{\Delta E}{k_B T}}}$$

where I_0 is the initial emission intensity, I(T) is the emission intensity at temperature T, A is a constant, k_B is the Boltzmann constant, and ΔE is the activation energy for the thermal quenching. A systematic increase of activation energy is observed in the $(Ba_{1-x}, Sr_x)_3Si_6O_9N_4$: Eu^{2+} phosphors as x increases, as shown in the inset of Fig. 9-a.

The change in local coordination around Eu^{2+} often facilitates the change of Stokes shift with x, which may account for the thermal quenching mechanism of $(\mathrm{Ba}_{1-x}, \mathrm{Sr}_x)_3\mathrm{Si}_6\mathrm{O}_9\mathrm{N}_4$: Eu^{2+} phosphors [35]. The Stokes shifts with x are shown in the inset of Fig. 9-a. An overall decreased Stokes shift is observed in $(\mathrm{Ba}_{1-x}, \mathrm{Sr}_x)_3\mathrm{Si}_6\mathrm{O}_9\mathrm{N}_4$: Eu^{2+} phosphors with increasing x. The configuration coordinate diagram is frequently used to explain the correlation between Stokes shift and thermal quenching. With decreasing Stokes shift, the thermal activation energy increases, implying that the nonradioactive transition probability decreases. This argument may apply to the $(\mathrm{Ba}_{1-x}, \mathrm{Sr}_x)_3\mathrm{Si}_6\mathrm{O}_9\mathrm{N}_4$: Eu^{2+} system given the general lower thermal quenching with increasing x.

In addition, the $(Ba_{1-x}, Sr_x)_3Si_6O_9N_4$: Eu^{2+} phosphors show a different emission peak shift with the increase of temperature depending on x. As shown in Fig. 9-b, the emission peak wavelength of $(Ba_{1-x}, Sr_x)_3Si_6O_9N_4$: Eu^{2+} phosphors shifts to longer wavelength with increasing temperature as x ranges from x=0 to x=0.4. This result can be explained by the Varshini equation [36]:

$$E(T) = E_0 - \frac{aT^2}{T+b}$$

where E(T) is the energy difference at a special temperature T, E_0 is its value at zero K, and A and A are constants. Therefore, it can be directly concluded that E(T) will decrease as a result of increasing temperature, causing an emission redshift. The emission peak wavelength of $(Ba_{1-x}, Sr_x)_3Si_6O_9N_4$: Eu^{2+} phosphors shifts to longer

wavelength (2–4 nm increase) when x ranges from x = 0 to x = 0.4. Inconsistently, the emission peak wavelength starts to shift to shorter wavelength (2 nm decrease) when x is more than 0.4. This transformation of redshift to blue-shift as increasing x can be explained by a configuration coordinate model as shown in Fig. 9-c. It is involved with the interaction between 5d electron of Eu²⁺ and thermally active phonon. The phonon mean free path in the crystal lattice will decrease, and the collision probability between 5d electron of Eu²⁺ and phonon will increase. When the temperature increases, more 5d electrons move from low energy state (Es1) to high energy state (Es2) by getting across the energy barrier (Δ E) through the thermally active phonon-assisted tunneling intersection, then return to the ground state (Gs), leading to a shorter wavelength emission. Therefore, it can be said that the emission peak blue shifts with an increase of temperature [37].

4. Conclusions

Using high-energy ball milling to mix and activate the raw materials, single phase (Ba, Sr) $_3$ Si $_6$ O $_9$ N $_4$: Eu $^{2+}$ phosphors were synthesized at a temperature as low as 1200 °C. The Ba $_3$ Si $_6$ O $_9$ N $_4$: Eu $^{2+}$ phosphor exhibited two different emission bands, ascribed to Eu in Ba3 and Ba2 site respectively. Theoretical calculation results indicated that Eu atoms preferentially occupy Ba3 site and explained the origination of weak 405 nm and strong 518 nm emission in the Ba $_3$ Si $_6$ O $_9$ N $_4$ crystal. DOS (Density of State) analysis revealed that the upper and lower states related to the luminescence properties are mainly induced by Ba and Eu atoms, respectively.

Sr/Ba substitution led to a redshift emission at the starting low Sr concentration, then a blueshift emission at the room temperature for higher Sr doping because of the overall competition effect of lattice contraction, second-sphere shrinkage and local structure disordering in (Ba, Sr)₃Si₆O₉N₄: Eu²⁺ phosphors. In addition, Sr/Ba substitution improved thermal quenching of (Ba, Sr)₃Si₆O₉N₄: Eu²⁺ phosphors and resulted in a different characteristic of emission peak shift with the increase of temperature.

Acknowledgements

This research was supported by the National Natural Science Foundation of China (Grant No. 51302029), the project-sponsored by OATF of UESTC and CSC (201506075055) and the Fundamental Research Funds for the Central Universities (Grant No. ZYGX2015J110).

Appendix A. Supplementary data

Supplementary data related to this article can be found at http://dx.doi.org/10.1016/j.jallcom.2016.05.009.

References

- R.J. Xie, H.T. Hintzen, Optical properties of (oxy)nitride materials: a review, J. Am. Ceram. Soc. 96 (2013) 665–687.
- [2] L.-J. Yin, W. Yu, X. Xu, L.-Y. Hao, A. Simeon, The effects of fluxes on AlN: Eu²⁺ blue phosphors synthesized by a carbothermal reduction method, J. Am. Ceram. Soc. 94 (2011) 3842–3846.
- [3] L.-J. Yin, G.-Z. Chen, Z.-Y. Zhou, X. Jian, B. Xu, J.-H. He, H. Tang, C.-H. Luan, X. Xu, J.R. van Ommen, H.T. Hintzen, Improved blue-emitting AlN: Eu²⁺ phosphors by alloying with GaN, J. Am. Ceram. Soc. 98 (2015) 3897–3904.
- [4] L.J. Yin, W. Yu, X. Xu, L.Y. Hao, Synthesis and photoluminescence of Eu, Mgalon phosphors by carbothermal reduction, J. Lumin. 132 (2012) 671–675.
- [5] R.J. Xie, N. Hirosaki, Silicon-based oxynitride and nitride phosphors for white LEDs - a review, Sci. Technol. Adv. Mater. 8 (2007) 588–600.
- [6] G. Chen, L.-J. Yin, J.-T. Dong, Y.-Y. Feng, Y. Gao, W. He, Y. Jia, X. Xu, H.T. Hintzen, Synthesis, Crystal structure, and luminescence properties of Y₄Si₂O₇N₂: Eu²⁺ oxynitride phosphors, J. Am. Ceram. Soc. 99 (2016) 183–190.
- [7] S. Lee, K.-S. Sohn, Effect of inhomogeneous broadening on time-resolved photoluminescence in CaAlSiN₃:Eu²⁺, Opt. Lett. 35 (2010) 1004–1006.
- [8] H.L. Li, R.J. Xie, N. Hirosaki, T. Takeda, G.H. Zhou, Synthesis and luminescence

- properties of orange-red-emitting $M_2Si_5N_8$: Eu^{2+} (M = Ca, Sr, Ba) light-emitting diode conversion phosphors by a simple nitridation of MSi_2 , Int. J. Appl. Ceram. Technol. 6 (2009) 459–464.
- [9] R.J. Xie, N. Hirosaki, K. Sakuma, Y. Yamamoto, M. Mitomo, Eu²⁺-doped Caalpha-SiAlON: a yellow phosphor for white light-emitting diodes, Appl. Phys. Lett. 84 (2004) 5404–5406.
- [10] Y.Q. Li, N. Hirosaki, R.J. Xie, T. Takeda, M. Mitomo, Crystal and electronic structures, crystal and electronic structures, luminescence properties of Eu²⁺-doped Si_{6-Z}Al_zO_zN_{8-Z} and M_ySi_{6-Z}Al_{z-Y}O_{z+Y}N_{8-Z-Y} (M=2li, Mg, Ca, Sr, Ba), J. Solid State Chem. 181 (2008) 3200–3210.
- [11] R.J. Xie, N. Hirosaki, T. Suehiro, F.F. Xu, M. Mitomo, A simple, efficient synthetic route to Sr₂Si₅N₈: Eu²⁺-based red phosphors for white light-emitting diodes, Chem. Mater. 18 (2006) 5578–5583.
- [12] R.J. Xie, N. Hirosaki, H.L. Li, Y.Q. Li, M. Mitomo, Synthesis and photoluminescence properties of beta-sialon: Eu²⁺ (Si_{6-z}Al_zO_zN_{8-z} : Eu²⁺), I. Electrochem. Soc. 154 (2007) 1314–1319.
- [13] H.-G. Kim, E.-H. Kang, B.-H. Kim, S.-H. Hong, Preparation and luminescence properties of $Ba_3Si_6O_9N_4$: Eu^{2+} phosphor, Opt. Mater. 35 (2013) 1279–1282.
- [14] L. Yu, Y. Hua, H. Chen, D. Deng, H. Wang, H. Ma, S. Xu, Luminescence properties of Ba₃Si₆O₉N₄:Eu²⁺ green-emitting phosphors for white leds, Opt. Commun. 315 (2014) 83–86.
- [15] C.X. Wu, S.G. Zhu, J. Ma, M.L. Zhang, Synthesis and formation mechanisms of nanocomposite WC-MgO powders by high-energy reactive milling, J. Alloys Compd. 478 (2009) 615–619.
- [16] C. Suryanarayana, Mechanical alloying and milling, Prog. Mater. Sci. 46 (2001) 1–184
- [17] J.S. Benjamin, Dispersion strengthened superalloys by mechanical alloying, Metall. Trans. 1 (1970) 2943–2951.
- [18] H. Hao, J. Liang, C. Li, L. Zhai, H. Zhou, B. Xu, Synthesis of YAG: Ce³⁺ phosphor by high energy milling and reactive sintering, Mater. Rev. 20 (2006).
- [19] X. Xu, T. Nishimura, N. Hirosaki, R.-J. Xie, Y. Zhu, Y. Yamamoto, H. Tanaka, New strategies for preparing NanoSized silicon nitride ceramics, J. Am. Ceram. Soc. 88 (2005) 934–937.
- [20] X. Xu, J. Tang, T. Nishimura, L. Hao, Synthesis of Ca-[alpha]-SiAlON phosphors by a mechanochemical activation route, Acta Mater. 59 (2011) 1570–1576.
- [21] L.-J. Yin, W.-J. Xie, X. Jian, Y.-Y. Feng, H. Tang, C.-H. Luan, Y.-L. Liang, C. Wang, X. Xu, Luminescent properties of a novel Al₁₀O₃N₈:Eu²⁺ phosphor by a mechanochemical activation route, Opt. Mater. 42 (2015) 511–515.
- [22] Y. Wang, X. Xu, L. Yin, L. Hao, High thermal stability and photoluminescence of Si–N-Codoped BaMgAl₁₀O₁₇:Eu²⁺ phosphors, J. Am. Ceram. Soc. 93 (2010) 1534–1536.
- [23] J.P. Perdew, K. Burke, M. Ernzerhof, Generalized gradient approximation made simple, Phys. Rev. Lett. 77 (1996) 3865–3868.
- [24] M. Segall, P.J. Lindan, M. Probert, C. Pickard, P. Hasnip, S. Clark, M. Payne, First-principles simulation: ideas, illustrations and the CASTEP code, J. Phys. Condens. Matter 14 (2002) 2717.
- [25] S.J. Clark, M.D. Segall, C.J. Pickard, P.J. Hasnip, M.I. Probert, K. Refson, M.C. Payne, First principles methods using CASTEP, Z. Krist. 220 (2005) 567–570.
- [26] H.J. Monkhorst, J.D. Pack, Special points for Brillouin-zone integrations, Phys. Rev. B 13 (1976) 5188–5192.
- [27] H. Watanabe, H. Yamane, N. Kijima, Crystal structure and luminescence of Sr_{0.99}Eu_{0.01}AlSiN₃, J. Solid State Chem. 181 (2008) 1848–1852.
- [28] Katsutoshi Komeya, Yi-Bing Cheng, Junichi Tatami, M. Mitomo, New green phosphor $Ba_3Si_6O_{12}N_2$:Eu for white led: crystal structure and optical properties, Key Eng. Mater. 403 (2009) 11–14.
- [29] J.-Y. Tang, J.-K. Gao, J.-H. Chen, L.-Y. Hao, X. Xu, M.-H. Lee, Contribution of cations to the photoluminescence properties of Eu-doped barium oxonitridosilicates phosphors, Comp. Mater. Sci. 79 (2013) 478–484.
- [30] P. Németh, L.A.J. Garvie, T. Aoki, N. Dubrovinskaia, L. Dubrovinsky, P.R. Buseck, Lonsdaleite is faulted and twinned cubic diamond and does not exist as a discrete material, Nat. Commun. 5 (2014).
- [31] Z. Xia, G. Liu, J. Wen, Z. Mei, M. Balasubramanian, M.S. Molokeev, L. Peng, L. Gu, D.J. Miller, Q. Liu, K.R. Poeppelmeier, Tuning of photoluminescence by cation nanosegregation in the (CaMg)_X(NaSc)_{1-X}Si₂O₆ solid solution, J. Am. Chem. Soc. 138 (2016) 1158–1161.
- [32] Y.Q. Li, J.E.J. van Steen, J.W.H. van Krevel, G. Botty, A.C.A. Delsing, F.J. DiSalvo, G. de With, H.T. Hintzen, Luminescence properties of red-emitting M₂Si₅N₈: Eu²⁺ (M=Ca, Sr, Ba) led conversion phosphors, J. Alloys Compd. 417 (2006) 273–279.
- [33] W.-Y. Huang, F. Yoshirnura, K. Ueda, W.K. Pang, B.-J. Su, L.-Y. Jang, C.-Y. Chiang, W. Zhou, D. Nguyen Hoang, R.-S. Liu, Domination of second-sphere shrinkage effect to improve photoluminescence of red nitride phosphors, Inorg. Chem. 53 (2014) 12822–12831.
- [34] S. Bhushan, M.V. Chukichev, Temperature dependent studies of cathodoluminescence of green band of ZnO crystals, J. Mater. Sci. Lett. 7 (1988) 319–321.
- [35] L.H. Liu, R.J. Xie, N. Hirosaki, T. Takeda, J.G. Li, X.D. Sun, Temperature dependent luminescence of yellow-emitting alpha-sialon:Eu²⁺ oxynitride phosphors for white light-emitting diodes, J. Am. Ceram. Soc. 92 (2009) 2668–2673.
- [36] Y.P. Varshni, Temperature dependence of the energy gap in semiconductors, Physica 34 (1967) 149–154.
- [37] L. Chen, C.-C. Lin, C.-W. Yeh, R.-S. Liu, Light converting inorganic phosphors for white light-emitting diodes, Materials 3 (2010) 2172–2195.